The Astrophysical Journal, 773:167 (9pp), 2013 August 20 doi:10.1088/0004-637X/773/2/167

CHARACTERISTIC LENGTH OF ENERGY-CONTAINING STRUCTURES AT THE BASE OF A CORONAL HOLE

V. I. Abramenko[1], G. P. Zank[2], A. Dosch[2], V. B. Yurchyshyn[1], P. R. Goode[1], K. Ahn[1], and W. Cao[1]
[1] Big Bear Solar Observatory, 40386 N. Shore Lane, Big Bear City, CA 92314, USA
[2] CSPAR, University of Alabama in Huntsville, Huntsville, AL, USA
Received 2013 February 7; accepted 2013 June 28; published 2013 August 6

ABSTRACT

An essential parameter for models of coronal heating and fast solar wind acceleration that rely on the dissipation of MHD turbulence is the characteristic energy-containing length $\lambda_\perp$ of the squared velocity and magnetic field fluctuations (u^2 and b^2) transverse to the mean magnetic field inside a coronal hole (CH) at the base of the corona. The characteristic length scale directly defines the heating rate. We use a time series analysis of solar granulation and magnetic field measurements inside two CHs obtained with the New Solar Telescope at Big Bear Solar Observatory. A data set for transverse magnetic fields obtained with the Solar Optical Telescope/Spectro-Polarimeter on board the *Hinode* spacecraft was utilized to analyze the squared transverse magnetic field fluctuations b_t^2. Local correlation tracking was applied to derive the squared transverse velocity fluctuations u^2. We find that for u^2 structures, the Batchelor integral scale λ varies in a range of 1800–2100 km, whereas the correlation length ς and the e-folding length L vary between 660 and 1460 km. Structures for b_t^2 yield $\lambda \approx 1600$ km, $\varsigma \approx 640$ km, and $L \approx 620$ km. An averaged (over λ, ς, and L) value of the characteristic length of u^2 fluctuations is 1260 ± 500 km, and that of b_t^2 is 950 ± 560 km. The characteristic length scale in the photosphere is approximately 1.5–50 times smaller than that adopted in previous models (3–30 $\times$ 10^3 km). Our results provide a critical input parameter for current models of coronal heating and should yield an improved understanding of fast solar wind acceleration.

Key words: Sun: corona – Sun: photosphere – Sun: surface magnetism – turbulence

Online-only material: color figures

1. INTRODUCTION

Solar magneto-convection in the photosphere and beneath gives rise to a broad spectrum of magnetohydrodynamic (MHD) waves, which carry energy (both kinetic and magnetic) from the base of the solar corona into its outer parts. There is no doubt that the propagation, absorption, interaction, and reflection of various types of MHD waves significantly contribute to the acceleration of solar wind (e.g., Matthaeus et al. 1999; Oughton et al. 1999; Thomas & Stanchfield 2000; Dmitruk et al. 2001; Bogdan et al. 2003; Cranmer & van Ballegooijen 2005; Cranmer et al. 2007; Verdini et al. 2010; Zank et al. 2012, to mention a few). To account for turbulent dissipation of MHD waves, a solution to the dissipative MHD equations is required, i.e., the dissipative term should be incorporated. The dissipative term, in turn, depends on a "free" parameter, namely, the characteristic energy-containing length $\lambda_\perp$ of the dynamical structures transverse to the mean magnetic field in a coronal hole (CH) at the base of the corona, where the fast solar wind emanates from (e.g., Matthaeus et al. 1999; Oughton et al. 1999; Dmitruk et al. 2001; Cranmer & van Ballegooijen 2005; Zank et al. 2012). The turbulent dissipation rate, responsible for heating and solar wind acceleration, is inversely proportional to $\lambda_\perp$, see Equation (8) in Dmitruk et al. (2001), Equation (56) in Cranmer & van Ballegooijen (2005), and Equation (16) in Zank et al. (2012).

The characteristic energy-containing length scale is an integral element underlying the decomposition of MHD fluctuations into high- and low-frequency components (Matthaeus et al. 1999; Zank et al. 2012). Indeed, within the existing models that exploit the dissipation of low-frequency turbulence to heat the solar corona, $\lambda_\perp$ plays perhaps the key role in determining the efficiency of heating. Rather surprisingly, almost nothing is known observationally about this critical parameter. Currently, only a very rough estimate of $\lambda_\perp$ was obtained based on the fact that the network spacing is about 3×10^4 km (or an order of magnitude less, Matthaeus et al. 1999; Dmitruk et al. 2001). Cranmer & van Ballegooijen (2005) introduced parameterized $\lambda_\perp$, which could be translated into 3 Mm near the base of the corona.

The goal of this work is to provide a better estimate for the energy-containing length scales using observed data on the transverse velocities and magnetic fields at the coronal base of a CH. We will analyze energy-containing structures of $u^2 = u_x^2 + u_y^2$ and b_t^2, where u_x and u_y are the transverse velocities, and b_t is the transverse component of the magnetic field in the photosphere inside a CH. The line-of-sight (LOS) component of the magnetic field is also analyzed for comparison purposes only.

2. DATA

We utilize data from the 1.6 m clear aperture New Solar Telescope (NST; Goode et al. 2010) operated at the Big Bear Solar Observatory (BBSO). High time cadence sequences of solar granulation images allowed us to calculate squared transverse velocities at the photospheric level ($\tau_{500} = 1$), whereas the co-temporal and co-spatial near-infrared magnetograms from the NST provided us with the LOS magnetic fields inside CHs. The squared transverse magnetic field fluctuations b_t^2 analyzed here were obtained from the Spectro-Polarimeter data at the Solar Optical Telescope (SOT/SP) on board the *Hinode* spacecraft (Kosugi et al. 2007; Tsuneta et al. 2008) acquired on 2007 March 10.

Two CHs for which NST time series were obtained are shown in Figure 1. Both CHs were observed at the times of their crossing the central meridian. The first CH was observed on 2011 August 12, and it is referred to hereafter as CH 2011-08-12.

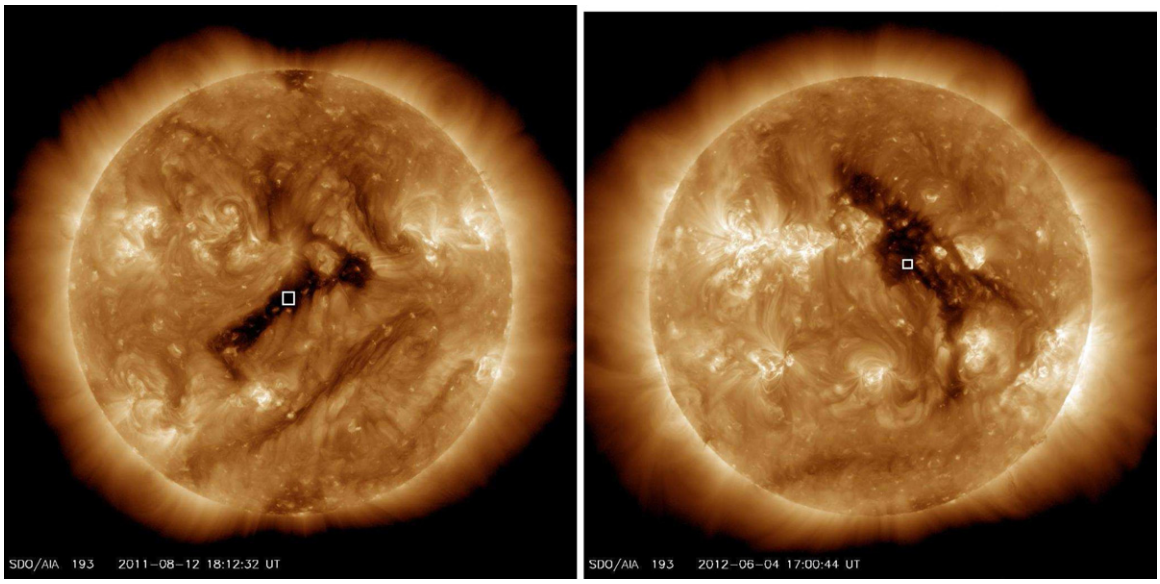

Figure 1. *SDO*/AIA/193 Å images showing the location of the two CHs observed on 2011 August 12 (left) and 2012 June 4 (right). The white boxes indicate the location of the NST FOV.

(A color version of this figure is available in the online journal.)

It was observed for nearly 20 minutes with a field of view (FOV) of $56'' \times 56''$. The second CH was observed with an FOV of $31'' \times 28''$ during about 2 hr on 2012 June 4 and is referred to hereafter as CH 2012-06-04.

The solar granulation data were acquired with a broad-band TiO filter centered at 705.7 nm with a band-pass of 1 nm (for details see Abramenko et al. 2012). The observations were aided with an adaptive optics (AO) system (Denker et al. 2007; Cao et al. 2010). To take maximal advantage of the AO system, only the central part of the entire FOV ($77'' \times 77''$) was utilized. The pixel scale of the PCO.2000 camera, $0\farcs0375$, was 2.9 times smaller than the telescope diffraction limit of 77 km. The Kiepenheuer-Institut für Sonnenphysik's software package for speckle interferometry (KISIP; Wöger & von der Lühe 2007) was applied to the 70 best images selected from a burst of 100 images to produce one speckle-reconstructed image at the diffraction limited resolution. After destretching and sub-sonic filtering (Abramenko et al. 2011) of the speckle-reconstructed images, the final CH 2011-08-12 (CH 2012-06-04) data set consisted of 82 (659) images. The final time cadence was 12 and 13 s, respectively. One-two minute gaps are sometimes present in the data. An example of a TiO/NST image of granulation is shown in Figure 2 (left).

Spatial fluctuations of the *transverse* component of the magnetic field inside a CH are of primary interest in this paper. Unfortunately, these kind of data are less plentiful, and the accuracy of measurements is much lower than that for the LOS data, especially in the quiet sun and in CHs. With this in mind, we address the problem in the following way. We utilized *Hinode*/SOT/SP data acquired inside a quiet sun region at the solar disk center on 2007, March 10. The processed data of the magnitude of the transverse magnetic field $B^T_{\rm app}$ and the corresponding LOS magnetic field $B^L_{\rm app}$ were kindly provided to us by Dr. B. Lites. The SOT/SP slit scanned an area of $304'' \times 164''$, or 220 × 120 Mm. The pixel size was $0\farcs150 \times 0\farcs160$. The data acquisition, processing, and noise issues are described in detail by Lites et al. (2008). The maps of the magnetic field components are shown in their Figure 2. We consider the $B^T_{\rm app}$ data set as the primary source for deriving the characteristic length of the transverse magnetic fluctuations. For comparison, we also calculated the λ, ς, and L from the LOS component $B^L_{\rm app}$.

We also utilized LOS magnetograms obtained for CH 2012-06-04 with the near-infrared imaging magnetograph (IRIM; Cao et al. 2010) installed on the NST. The spectro-polarimeter uses the Fe I spectral line at 1.56 μm and is based on a 2.5 nm interference filter, a 0.25 Å birefringent Lyot filter (Wang et al. 2000), and a Fabry-Pérot etalon, and provides a bandpass of ∼0.01 nm over an FOV of $50'' \times 25''$ with a pixel scale of $0\farcs098$. Based on the advantages of the near-IR window and the NST adaptive optics, IRIM provides solar spectro-polarimetry data with a Zeeman sensitivity of $10^{-3} I_c$, a diffraction limited resolution of $0\farcs2$, and a time cadence of 45 s (for full Stokes profiles). The raw IRIM data were processed to take into account dark and flat field corrections and polarization calibration (Cao et al. 2010; Goode et al. 2011; Cao et al. 2011). The linear polarization signal (the source of the transverse magnetic field data) from IRIM is very weak in CHs, therefore noise issues precluded scientific use of it, while the LOS magnetic field component was reliably derived by using the weak-field approximation. The best 34 LOS magnetograms (Figure 2, right) were utilized here to estimate the characteristic length of b_z.

3. TRANSVERSE VELOCITIES ACQUISITION

To derive transverse velocities in the photosphere, we applied the local correlation tracking (LCT) routine to the time series of solar granulation. The routine was first proposed by November & Simon (1988) and later modified and improved (e.g., Title et al. 1995; Hurlburt et al. 1995; Strous et al. 1996; Welsch et al. 2007; Chae & Sakurai 2008; Matloch et al. 2010; Verma & Denker 2011; Verma et al. 2013).

Matloch et al. (2010) tested the performance of the LCT on simulated data for quiet-sun granulation. The used LCT code is described in Welsch et al. (2007). The authors found that the LCT-derived velocities were approximately two times smaller than those derived directly from the simulations. The agreement between the simulated and LCT velocities was found to depend on the depth in the simulation box. The correlation reaches

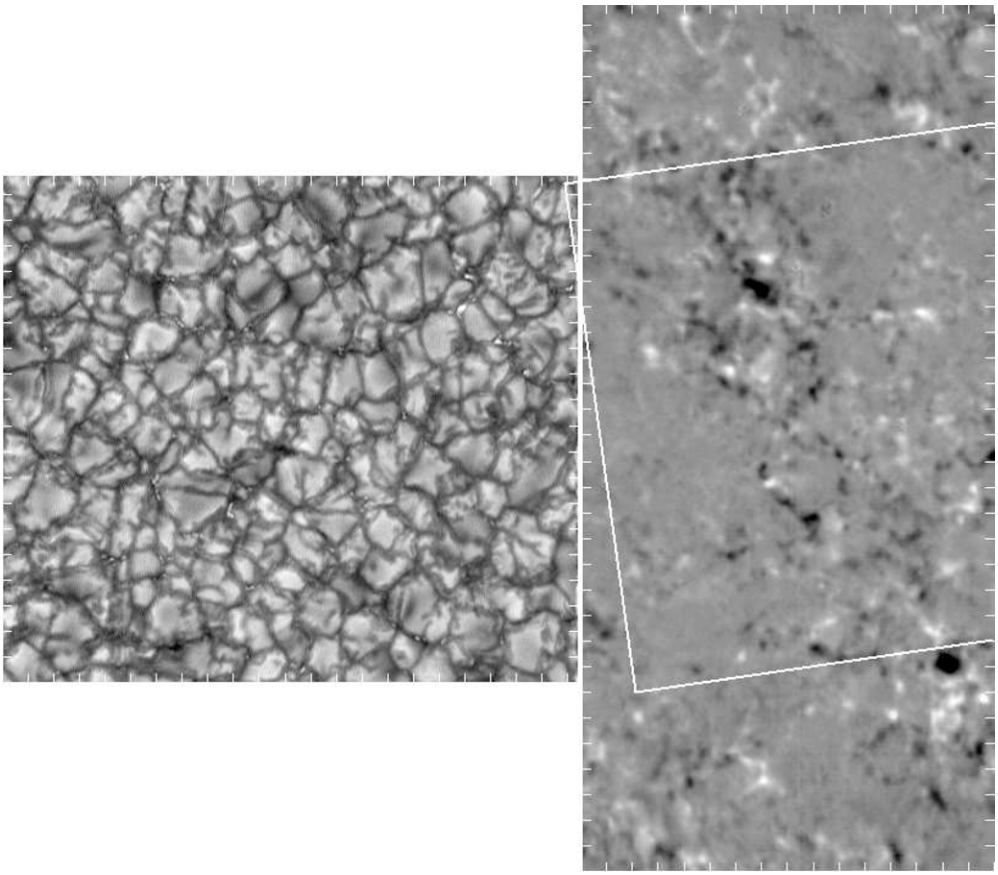

Figure 2. Left: one of the 659 images of CH 2012-06-04 obtained with the NST/TiO filter. Right: the co-temporal NST/IRIM LOS magnetogram. The white lines outline three boundaries of the FOV/TiO. The magnetogram is scaled from −100 G (black) to 100 G (white). The magnetogram and the granulation are shown in the same scale. The ticks separate a distance of 1 Mm.

maximum (∼0.65) at the depth close to the optical depth of $\tau = 1$, i.e., near the continuum formation level.

Verma & Denker (2011) and Verma et al. (2013) presented a comprehensive study of the accuracy and reliability of the LCT technique by applying it to *Hinode G*-band images. They demonstrated (Verma & Denker 2011) that the choice of three essential input parameters (time cadence, δt, accumulation interval, T, and the FWHM of a Gaussian sampling window, W) may significantly affect the result. Verma et al. (2013) evaluated the LCT technique using CO5BOLD simulations of solar granulation (Freytag et al. 2012). Note that the spatial and temporal resolution (28 km pixel scale and 10 s lowest time cadence) of the simulated data set are comparable to those of the observed NST set analyzed here (27 km pixel scale and 12–13 s time cadence). Verma et al. (2013) found that when multiplied by a factor of three, the frequency distribution of the LCT velocities demonstrates a very good agreement with the distribution of the velocities derived directly from the simulated set (see Figure 13 in Verma et al. 2013). Furthermore, Figure 7 in Verma et al. (2013) suggests that the time cadence of 10–30 s and the apodization window of 600–1000 km are the best choice for analysis of the inter-granular dynamics. Interestingly, the narrower window of 400 km results in the diminishing of the LCT velocities and degradation of the fine structures in the velocity pattern, so that the LCT technique fails to capture the inter-granular dynamics there.

Figures 4–6 in Verma et al. (2013), as well as Figure 3 in Verma & Denker (2011) demonstrate that the extension of the accumulation interval T results in the diminishing of the LCT velocities as well. The authors found that in order to reveal the persistent (e.g., meso-granular and/or super-granular) flows in the solar granulation, the accumulation time should be no less than approximately 20 minutes. One might conclude that shorter time intervals should be employed to reveal inter-granular dynamics.

Here we focus on the analysis of inter-granular dynamics, i.e., on proper motions of granule edges, mini-granules (Abramenko et al. 2012), inter-granular bright points, and filigree-like features. According to MHD simulations (R. Stein 2013, private communication) and NST observations, these features visible inside inter-granular lanes are mostly associated with strong quiet Sun magnetic fields. It is thought that Alfvén waves are generated by rapid displacements of magnetic footpoints driven by these inter-granular flows and the energy-containing scale should be related to this kind of motions. We will choose the LCT configuration parameters based on the above considerations and the results of Verma & Denker (2011) and Verma et al. (2013).

The version of the LCT used here was elaborated by Strous (1994) and Strous et al. (1996) and utilizes the ANA software package.[3] We start with choosing the best time cadence δt using the CH-2012-06-04 data recorded with time cadence of 13 s. We generated two additional sets with $\delta t \approx 39$ and 65 s by selecting each third and fifth image, respectively. In this case, with $T = 10$ minutes and $W = 540$ km, we obtained the following values of the square root of the averaged squared velocities: 1.21 km s^{-1}

[3] See more at http://ana.lmsal.com/ana/.

for $\delta t = 13$ s, 0.61 km s^{-1} for $\delta t = 39$ s, and 0.26 km s^{-1} for $\delta t = 65$ s. We thus concluded that the first estimate of the LCT velocity (1.21 km s^{-1} derived for $\delta t = 13$ s) is the best choice because it is the largest one out of the three and the closest one to the estimates derived by Verma et al. (2013, see Figure 8) for the range of $\delta t = 10$–30 s and $W = 600$–1000 km.

The next critical parameter is the FWHM of the Gaussian sampling window W. According to Verma & Denker (2011) and Verma et al. (2013), the choice of W must be guided by the spatial scales of the studied dynamic events. In the case of the inter-granular scale events, the window should not exceed the typical size of a granule, i.e., ~1000 km. We thus tested three choices of W: 10 × 10 pixels (270 km in linear extent), 20 × 20 pixels (540 km), and 40 × 40 pixels (1090 km), for which we obtained the following square root of the averaged squared velocities: 1.02 km s^{-1} for $W = 270$ km, 1.21 km s^{-1} for $W =$ 540 km, and 1.11 km s^{-1} for $W = 1090$ km. Again, we chose the $W = 540$ km value since it ensures the largest detected velocities.

Finally, the accumulation (averaging) time interval T should be shorter than 20 minutes. Similarly, four choices of T were tested: 2, 5, 10, and 20 minutes. The following square roots of the averaged squared velocities were obtained: 1.71, 1.40, 1.21, and 1.06 km s^{-1}, respectively. Qualitatively, the tendency here agrees with that reported by Verma & Denker (2011) and Verma et al. (2013): the averaged velocity decreases as T increases. However, there is no indication which one might be closer to the real value. The possible answer is that all of them are true, and they simply reflect the dynamics on different time scales. We, therefore, decided to proceed using all of the above accumulation intervals.

As we saw above, underestimation of the LCT velocities by two to three times is an unavoidable shortcoming of the LCT technique. However, in this particular study, we are focused on calculation of the correlation functions characterizing LCT velocities structures rather than on the magnitude of the velocities. According to the general expression of the correlation function (see Equation (1) below), multiplying the velocity (or squared velocities) by a constant factor does not change the correlation function (the factor evenly appears in the numerator and the denominator of the right-hand part of Equation (1)).

Note that the TiO spectral line is formed in the quiet sun at optical depths of $\tau = 1$, i.e., near the continuum level (Abramenko et al. 2012; Berdyugina et al. 2003), where the LCT is expected to perform in the most reliable way (Matloch et al. 2010).

4. DIFFERENT METHODS TO DERIVE THE CHARACTERISTIC LENGTH

Our main goal is to find, following Batchelor (1953, page 47), "convenient measures of the linear extent of the region within which velocities [as well as squared velocities and magnetic field] are appreciably correlated." For an arbitrary two-dimensional (2D) scalar field $v(\mathbf{r})$, a general definition of the correlation function $B(\mathbf{r})$ reads as (Jenkins & Watts 1969; Monin & Yaglom 1975)

$$B(r) = \langle (v(\mathbf{x}+\mathbf{r}) - \langle v \rangle) \cdot (v(\mathbf{x}) - \langle v \rangle) \rangle / \sigma^2, \quad (1)$$

where $\mathbf{r}$ is a separation vector, $\mathbf{x} \equiv (x, y)$ is the current point on an image, and σ^2 is the variance of v. Angle brackets denote averaging over the area of an image. Based on $B(\mathbf{r})$, the characteristic length of the field v can be defined as a distance where some correlation in v holds.

We will use three different approaches for deriving the characteristic length from the correlation function $B(r)$. For a noise-free smooth image, measured on a large enough area, all of our approaches produce the same magnitude for the characteristic length. However, in case of real data, the estimates from different methods might differ. We will consider the results obtained from these approaches as independent estimates of the characteristic length for a given image.

The first approach is to determine the integral scale (Batchelor 1953)

$$\lambda = \int_0^{r_{\max}} B(r) dr, \quad (2)$$

which has also been used in the formulation/derivation of the turbulence transport model of Zank et al. (2012). Here, the integration is supposed to be performed over all scales up to infinity. However, in the case of real data, at scales exceeding a certain large distance, data noise might cause a non-diminishing $B(\mathbf{r})$, thus resulting in an artificially large integral scale. To mitigate this problem, the signal in pixels was assigned to be zero when the absolute value of the measured signal was below one standard deviation. Moreover, we noticed that in our data sets, an increase in correlation is observed at scales larger than approximately 5 Mm, which is caused by the presence of adjacent features in a studied field. To avoid an overestimation of the integral length, we adopted $r_{\max}$ in Equation (2) to be 5 Mm.

The second method is to approximate the correlation function near the origin (Hinze 1959; Monin & Yaglom 1975; Feder 1989):

$$B(r) = \text{Const} \cdot \exp(-r/\varsigma). \quad (3)$$

Thus, when $B(r)$ is fitted with an exponential function, the correlation function drops by e times at a scale ς. This scale is called the correlation length in the percolation (Feder 1989) and in second-order phase transition[4] theories.

Finally, the characteristic length can also be determined via the e-folding scale of $B(r)$ without any approximation of the latter (the scale, where the *measured* correlation function drops by e times). We denote this measure as L.

The parameters introduced above λ, ς, and L are considered as proxies for the characteristic length, and were calculated for all data sets.

5. RESULTS

5.1. Characteristic Length of Transverse Velocity Fluctuations

Dividing the resulting LCT displacements in each pixel by the accumulation time T, we obtained components of the transverse velocities U_x and U_y (flow maps). We then computed the probability distribution functions (PDFs; Figure 3) of U_x and U_y for each flow map, which showed that the alignment of the images in the data sets was very good, and there are no large-scale systematic shifts, so that residual large-scale velocities (mean velocities) are negligible. Indeed, the PDFs of the U_x and U_y components are well centered at zero and are distributed in accordance with a Gaussian function. The mean velocity components $\langle U_x \rangle$ and $\langle U_y \rangle$ do not exceed 35 m s^{-1} in any flow map. After subtraction of the mean velocities from the flow maps, we obtained the velocity fluctuations maps u_x and u_y. A fragment of a u_x, u_y map is shown in Figure 4, left. Centers of large granules are usually places of slow transverse motions, whereas the majority of long arrows are located near

[4] http://staff.science.nus.edu.sg/~parwani/c1/node52.html

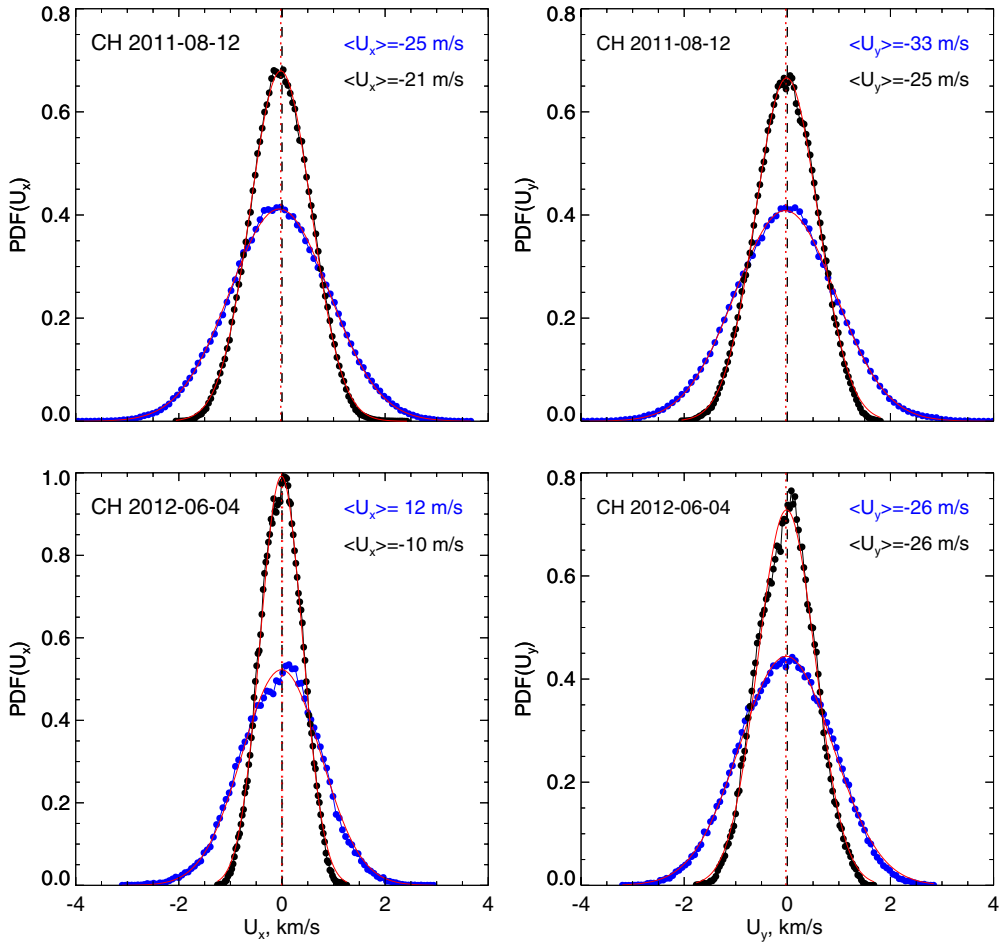

Figure 3. Probability distribution functions (PDFs) of the transverse velocities, U_x (left) and U_y (right) derived from a velocity map for CH 2011-08-12 (top; 734 × 734 data points) and CH 2012-06-04 (bottom; 351 × 351 data points). PDFs, obtained with the accumulation time interval $T = 2$ (20) minutes are shown with blue (black) circles. The red curves are the best Gaussian fit to the data points. The mode of the Gaussian fit is shown for each data set with the same color code. The Gaussian mode deviates from zero by less than 35 m s^{-1} for all flow maps.

(A color version of this figure is available in the online journal.)

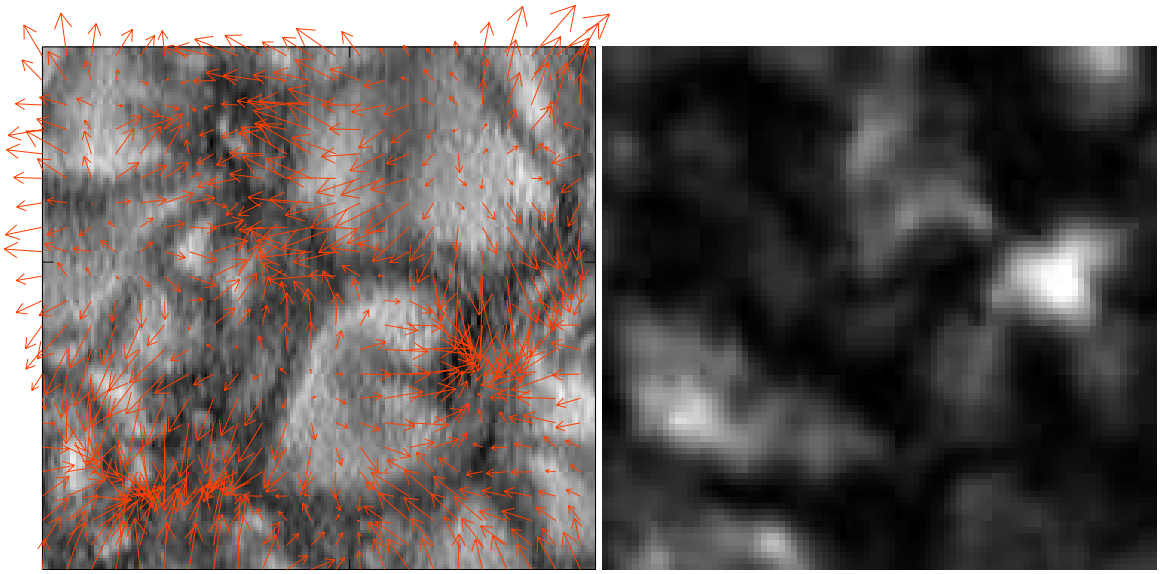

Figure 4. Left: NST/TiO image of solar granulation inside CH 2012-06-04 overplotted with the corresponding velocity fluctuations map (arrows) obtained with $T =$ 10 minutes. The image size is 4.9 × 4.6 Mm. The length of the arrows is in proportion to the velocity, and the longest arrows correspond to 2.2 km s^{-1}. Right: the corresponding map of squared transverse velocity fluctuations, u^2, saturated at 4 km^2 s^{-2}.

(A color version of this figure is available in the online journal.)

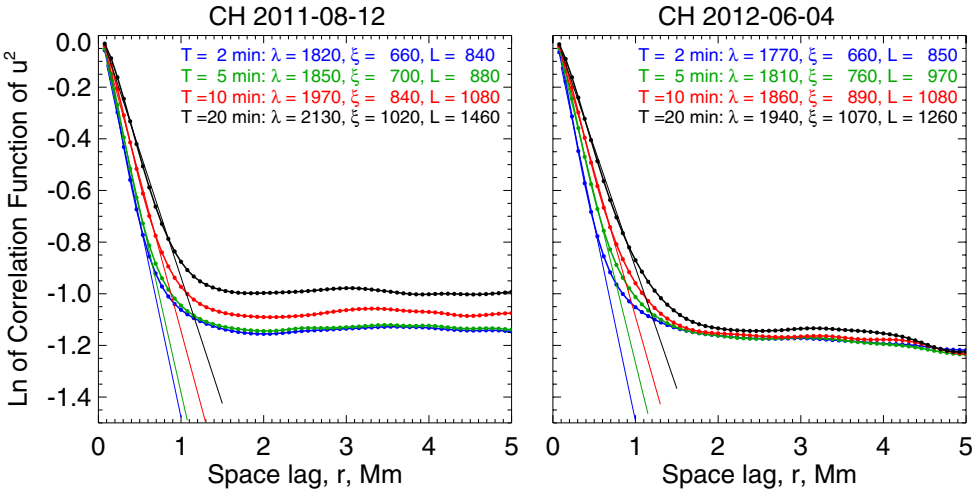

Figure 5. Plotted is the natural logarithm of the correlation function of u^2 vs. the spatial lag r for the two CHs. The circles denote the data points and the straight lines are best linear fits to the first 8–10 data points used to derive ς according to Equation (3). The color code refers to the accumulation time intervals of 2 (blue), 5 (green), 10 (red), and 20 (black) minutes. The values of the integral length λ the correlation length ς and the e-folding length L in km are shown.

(A color version of this figure is available in the online journal.)

Table 1
Characteristic Lengths of the Squared Transverse Velocity Fluctuations, u^2

	λ, km	ς, km	L, km
CH 2011-08-12			
$T = 2$ minutes	1820	660	840
$T = 5$ minutes	1850	700	880
$T = 10$ minutes	1970	840	1080
$T = 20$ minutes	2130	1020	1460
CH 2012-06-04			
$T = 2$ minutes	1770	660	850
$T = 5$ minutes	1810	760	970
$T = 10$ minutes	1860	890	1080
$T = 20$ minutes	1940	1070	1260
$\langle\lambda_\perp\rangle$	1890 ± 120	830 ± 160	1050 ± 220

the periphery of large granules and inside inter-granular lanes, thus supporting the idea of enhanced dynamics in inter-granular lanes and proving the capability of the LCT to detect it.

We first focus on the statistical properties of the squared amplitude $u^2 = (u_x^2 + u_y^2)$ of the (u_x, u_y) vector, which is a positive scalar that characterizes the kinetic energy of photospheric random motions driven by convection and turbulence. Therefore, the u^2 maps represent an entity in which we are interested (see Equations (2)–(6) in Zank et al. 2012). In the right panel of Figure 4, we show a u^2 map calculated from the flow map shown in the left panel. Patches of enhanced kinetic energy (white areas) are intermittent with dark voids. Our aim is to estimate the characteristic length of these patches.

Figure 5 shows the correlation functions of u^2 structures determined with different accumulation intervals T. All the proxies of the characteristic length λ, ς, and L (see Section 4) show an increase with larger T, which seems to be expected because various small-scale velocity patterns tend to be smeared as they are averaged over time longer time intervals (Table 1.) The estimate of the Batchelor integral length λ is the largest. For all cases, ς is less than L. Based on the three proxies, the characteristic length of u^2 varies in the range of 660–2130 km with an average value of 1260 ± 500 km.

We then calculated correlation functions of the transverse velocity components u_x and u_y. For a 2D vector field (unlike a scalar field), one has to compute two correlation functions (Batchelor 1953): one of them, B_p, is parallel to the separation vector $\mathbf{r}$, and the other one, B_n, is normal to $\mathbf{r}$. To simplify the calculations without sacrificing the quality, we computed $B_p(u_x)$ assuming that r varies along the x-axis only. $B_n(u_x)$ was computed with r varying along the y-axis. The correlation functions for u_x are shown in Figure 6. Similarly, we computed both correlation functions for u_y, which were very similar to that derived for u_x, so their plots are not shown. The averaged (over T and both CHs) values of λ, ς, and L obtained from the plots are gathered in Table 2.

The averaged integral length λ derived for both CHs using u_x and u_y from the parallel correlation functions $B_p(u_x)$, $B_p(u_y)$ is 720 ± 160 km, whereas λ calculated from the normal correlation functions is 1380 ± 230 km. Both are smaller than λ obtained from $B(u^2)$. This can be understood from the non-negative nature of the u^2 field, which gives an extended positive tail for $B(u^2)$. This is not the case for the parallel and normal correlation function of the alternating-sign fields of u_x and u_y. The correlation length ς and the e-folding length L from u_x, u_y agree within the error bars with that derived from u^2.

We find that the behavior of the parallel and normal correlation functions is different (see Figure 7). Whereas the normal correlation function B_n is positive for all scales, the parallel function changes sign, always situated below the normal correlation function; i.e., $B_p(r) < B_n(r)$. This situation holds for all the analyzed data sets and for both velocity components u_x and u_y. On average, the parallel correlation function has a characteristic length of 800 ± 160 km, whereas the characteristic length derived from the normal correlation function is 1310 ± 280 km. Note that in the case of homogeneous isotropic hydrodynamical turbulence, the mutual behavior of the parallel and normal correlation functions of velocity fluctuations is expected to be quite the opposite, i.e., the parallel correlation function exceeds the normal correlation function at all scales: $B_p(r) > B_n(r)$ (Batchelor 1953; Monin & Yaglom 1975). Obviously, the condition of homogeneous isotropic turbulence is not met in the solar photosphere. Moreover, the presence of magnetic fields could also contribute in the observed peculiar relationship between the correlation functions.

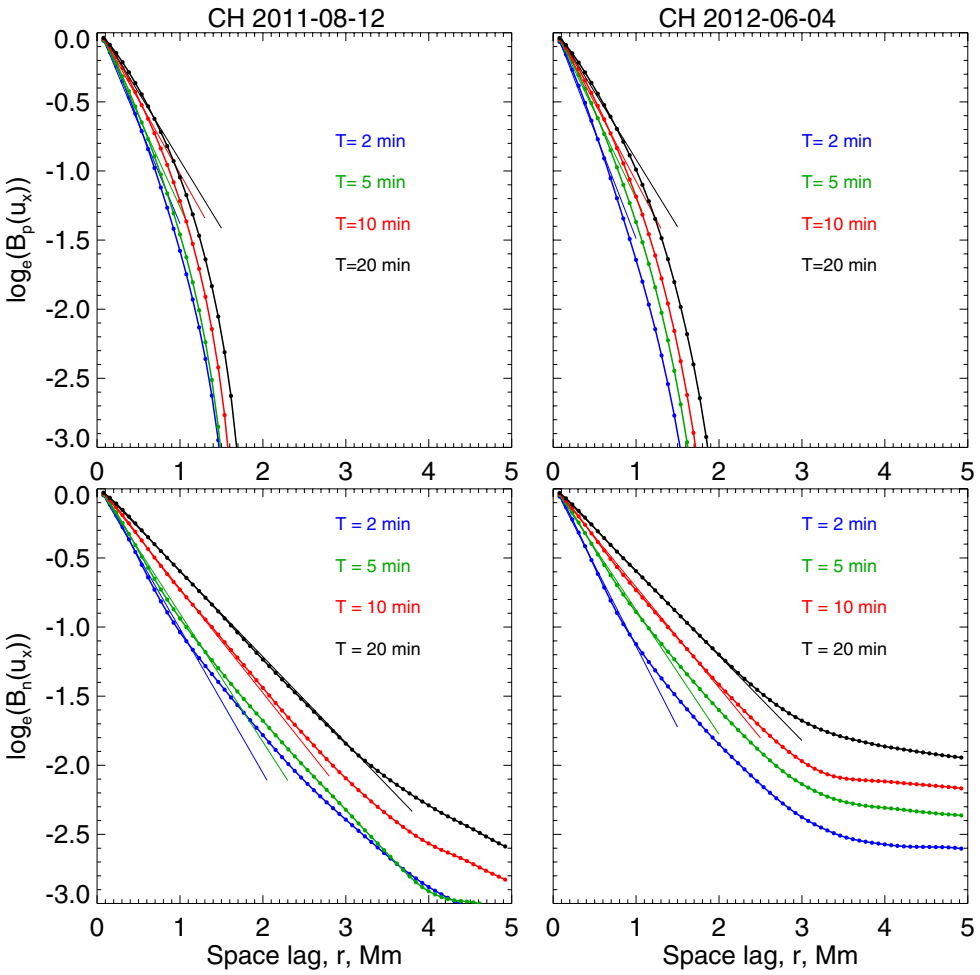

Figure 6. Plotted is the natural logarithm of the parallel (upper row) and normal (bottom row) correlation functions for u_x vs. the spatial lag r. The notation is the same as in Figure 5.

(A color version of this figure is available in the online journal.)

Table 2
Averaged Characteristic Lengths of the Components u_x and u_y from the Parallel $B_p(r)$ and Normal $B_n(r)$ Correlation Functions

	λ, km	ς, km	L, km	λ, km	ς, km	L, km
	u_x			u_y		
$\langle\lambda_\perp\rangle$ for $B_p(r)$	650 ± 100	840 ± 140	830 ± 120	800 ± 190	860 ± 160	850 ± 140
$\langle\lambda_\perp\rangle$ for $B_n(r)$	1340 ± 230	1240 ± 290	1260 ± 300	1430 ± 250	1270 ± 320	1300 ± 320

5.2. Characteristic Length of the Magnetic Field Fluctuations

The correlation functions from the squared magnetic field components are shown in Figure 8. The most interesting to us is the correlation function of the squared transverse magnetic field component b_t^2 plotted with the green line. On scales below approximately 0.5 Mm, the three correlation functions are similar. On larger scales, the NST b_z^2 function (red line) agrees well with that derived from b_t^2. (The estimates for λ, ς, and L derived from the green and red curves are similar too.) It is plausible that the very low noise level in the $B^L_{\rm app}$ data (about 2–3 G; Lites et al. 2008) is the reason why on scales larger than 1 Mm the blue curve in Figure 8 is much lower than the green and red curves. Thus, the correlation functions from the squared LOS component of the magnetic field can be used as an appropriate proxy to estimate the correlation function of the squared transverse component. The characteristic length of the squared transverse magnetic field fluctuations varies in a range of 617–1600 km with an average value of 950 ± 560 km.

When comparing the characteristic lengths derived for u^2 with those derived for b_t^2, we find that for the integral length $\lambda(u^2)/\lambda(b_t^2) \approx 1.2$ for the correlation length $\varsigma(u^2)/\varsigma(b_t^2) \approx 1.3$ and for the e-folding length $L(u^2)/L(b_t^2) \approx 1.7$. Thus, the characteristic scale of the squared velocity fluctuations is larger than that of the squared transverse magnetic field.

In Figure 9, we compare the b_z^2-correlation functions derived from the magnetic field data obtained with *SDO*/HMI (pixel scale 0.″5), *Hinode* SOT/FG (pixel scale 0.″16), and NST/IRIM (pixel scale 0.″098) instruments for the same area inside the CH-2011-08-12. The figure demonstrates that the correlation function becomes narrower and produces smaller estimates of the characteristic length as the spatial resolution improves.

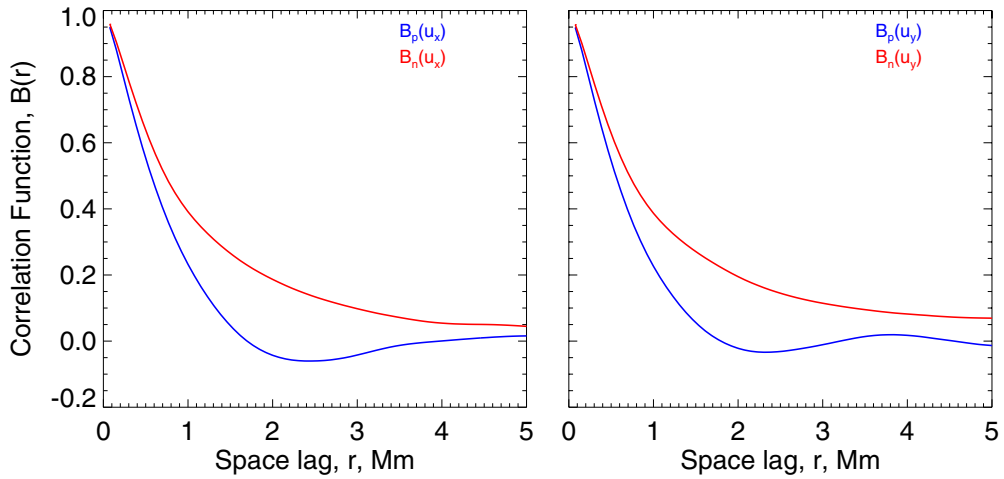

Figure 7. An example of the parallel (blue) and normal (red) correlation functions calculated from u_x (left) and u_y (right) components of the transverse velocity fluctuations. The data for CH-2011-08-12 obtained with the accumulation time of $T = 5$ minutes are used for these plots.

(A color version of this figure is available in the online journal.)

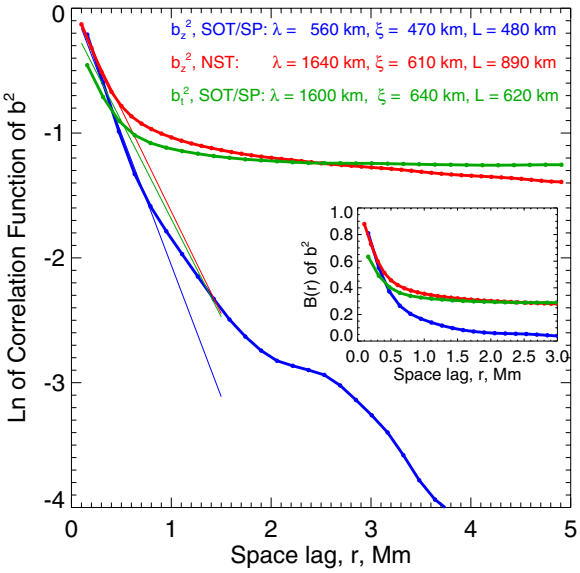

Figure 8. Plot of the natural logarithm of the correlation function of b^2 vs. the spatial lag r. The circles denote the data points, and the straight lines are the best linear fits to the first data points used to derive the values of ς from Equation (3). The insert shows this plot with linear axes.

(A color version of this figure is available in the online journal.)

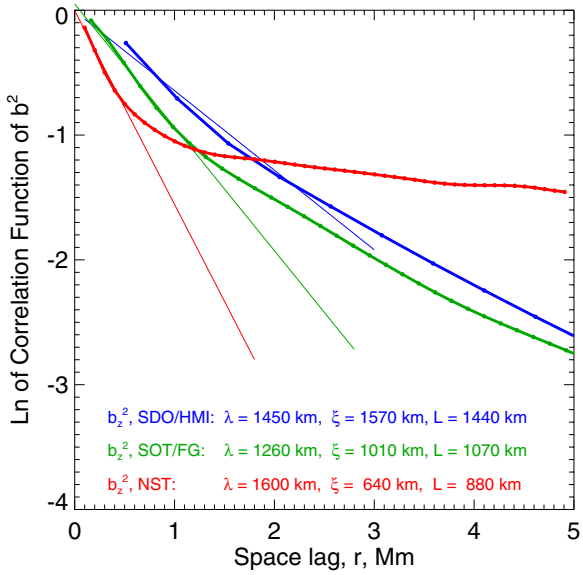

Figure 9. Plot of the natural logarithm of the correlation function of b_z^2 vs. the spatial lag r for the same area on the Sun (the CH 2011-08-12) but derived from data acquired with different instruments. The notation is the same as in Figure 8.

(A color version of this figure is available in the online journal.)

6. CONCLUSIONS AND DISCUSSION

Using high spatial (0.″1) and temporal (12–13 s) resolution time series of solar granulation acquired inside two CHs with the NST at BBSO, we computed the characteristic (correlation) length of the transverse velocity fluctuations u^2. The corresponding length of the transverse magnetic field fluctuations b_t^2 was derived from a unique and high quality *Hinode* SOT/SP data set that covered a large area of 220 × 120 Mm.

The characteristic length of the energy-containing structures u^2 and b_t^2 was derived from correlation functions of u^2 and b_t^2 by using three independent methods. These were calculated from the Batchelor integral scale λ, the correlation length ς, and the e-folding length L.

For u^2 structures, Batchelor integral scale λ varies in the range of 1800–2100 km, whereas values of ς and L vary between 660 and 1460 km. The structures for b_t^2 yield Batchelor integral scale as $\lambda \approx 1600$ km, a correlation length as $\varsigma \approx 640$ km, and an e-folding length as $L \approx 620$ km. The averaged (over λ, ς, and L) characteristic scale for the u^2 fluctuations is 1260 ± 500 km, and that for b_t^2 is 950 ± 560 km.

The above results show that the characteristic length derived from squared velocity fluctuations exceeds that derived from the squared transverse magnetic field fluctuations by 20%–70%.

By analyzing the correlation functions of the velocity components u_x and u_y, we found that the normal and parallel correlation functions are different. For the case of isotropic hydro-dynamical turbulence $B_p(r) > B_n(r)$, whereas the correlation functions observed here are in the opposite sense, i.e., $B_p(r) < B_n(r)$ at all observable scales. The discrepancy might be attributed to the presence of the magnetic field and/or violation of the isotropy. The parallel correlation function yields a characteristic length for the velocity fluctuations of 803 ± 157 km, whereas the characteristic length derived from the normal correlation function is 1307 ± 278 km.

As the spatial resolution improves, the correlation function for b_z^2 becomes narrower and yields smaller estimates of the characteristic length. Since the correlation functions of b_z^2 and b_t^2 are similar, one might expect that with improved solar instruments, b_t^2 might well produce smaller estimates for $\lambda_\perp$. Thus, we may perhaps regard the magnitudes of $\lambda_\perp$ reported here as an upper limit only.

Certainly, the study described here warrants further investigation using better magnetic field data. For example, the velocity and transverse magnetic field measurements should refer to a CH area, whereas in this study, the transverse magnetic field fluctuations were obtained for a quiet sun region. However, we may be obtaining realistic estimates because, as it is shown in Figure 8, the correlation functions for CH and the quiet sun areas are rather similar and produce similar estimates of the characteristic length. It would also be useful to compare the LCT results with those derived from the tracking of magnetic elements. This task requires high cadence and a long series of magnetic fields measured inside CHs, and is left for a future study.

We have shown that the characteristic length of the energy-containing structures in the photosphere lies in the range of 600–2000 km, which is on average an order of magnitude lower than the values used currently in models (e.g., Matthaeus et al. 1999; Dmitruk et al. 2001). Taking into account that the nonlinear dissipation terms in the MHD equations (Equation (1) in Zank et al. 2012) are inversely proportional to the correlation length of energy-containing structures at the base of the corona (see Equation (16) in Zank et al. 2012), our results here play a critical role in determining the effectiveness of the coronal turbulence transport models in heating the solar corona, and hence in driving the solar wind.

It is worth noting that obtained estimates of the averaged transverse velocity (about 1.2 km s^{-1}) and the characteristic length scale for u^2 fluctuations (about 1300 km), combined with the results of Rüdiger et al. (2011), allowed us to evaluate the turbulent magnetic diffusivity and cross-helicity in the photosphere. Indeed, when the above estimates are used in the expression for turbulent magnetic diffusivity $\eta_T \approx u_{\rm rms} l/3$, it gives us $\eta_T \approx 500 \pm 200$ km^2 s^{-1} (5×10^{12} cm^2 s^{-1}). In turn, the cross-helicity, according to Equations (19) and (24) in Rüdiger et al. 2011, is in direct proportion with η_T. This allows us to conclude that the magnitude of the cross-helicity (1 G km s^{-1}) obtained by Rüdiger et al. (2011) with $\eta_T = 1 \times 10^{12}$ cm^2 s^{-1}, might be at least five times larger. The importance of the cross-helicity for estimation of internal solar parameters needed for dynamo was emphasized by Kuzanyan et al. (2007) and Pipin et al. (2011).

It is interesting that the magnitude of the turbulent magnetic diffusivity obtained here in a CH for the spatial scale of ~1300 km coincides with the value of η_T inferred from the spectrum of the turbulent diffusion coefficient in a CH on scale of 1000–1300 km (460–560 km^2 s^{-1}), reported by Abramenko et al. (2011, see Figure 10 there). Thus, our present results indirectly support the previous inference that the turbulent diffusivity is a scale-dependent parameter. Additionally, the agreement between two independent estimates of η_T argues for the reliability of the LCT technique.

We thank the anonymous referee, whose careful reading and comprehensive reports with critical comments significantly improved the paper. We are thankful to Dr. B. Lites for offering the processed SOT/SP data, to Drs. B. Vazquez, D. Hathaway, C. Smith for helpful discussion of these results. BBSO team efforts were supported by NSF (AGS-1146896, and ATM-0847126), NASA (NNX11AO73G), and AFOSR (FA9550-12-1-0066) grants.

REFERENCES

Abramenko, V. I., Carbone, V., Yurchyshyn, V., et al. 2011, ApJ, 743, 133
Abramenko, V. I., Yurchyshyn, V. B., Goode, P. R., Kitiashvili, I. N., & Kosovichev, A. G. 2012, ApJL, 756, L27
Batchelor 1953, The Theory of Homogeneous Turbulence (Cambridge: Cambridge Univ. Press)
Berdyugina, S. V., Solanki, S. K., & Frutiger, C. 2003, A&A, 412, 513
Bogdan, T. J., Carlsson, M., Hansteen, V. H., et al. 2003, ApJ, 599, 626
Cao, W., Ahn, K., Goode, P. R., et al. 2011, in ASP Conf. Ser. 437, Solar Polarization 6, ed. J. R. Kuhn, D. M. Harrington, H. Lin, S. V. Berdyugina, J. Trujillo-Bueno, S. L. Keil, & T. Rimmele (San Francisco, CA: ASP), 345
Cao, W., Gorceix, N., Coulter, R., et al. 2010, AN, 331, 636
Chae, J., & Sakurai, T. 2008, ApJ, 689, 593
Cranmer, S. R., & van Ballegooijen, A. A. 2005, ApJS, 156, 265
Cranmer, S. R., van Ballegooijen, A. A., & Edgar, R. J. 2007, ApJS, 171, 520
Denker, C., Tritschler, A., Rimmele, T. R., et al. 2007, PASP, 119, 170
Dmitruk, P., Milano, L. J., & Matthaeus, W. H. 2001, ApJ, 548, 482
Feder, J. 1989, Fractals (New York: Plenum Press)
Freytag, B., Steffen, M., Ludwig, H.-G., et al. 2012, JCoPh, 231, 919
Goode, P. R., Cao, W., Ahn, K., Gorceix, N., & Coulter, R. 2011, in ASP Conf. Ser. 437, Solar Polarization 6, ed. J. R. Kuhn, D. M. Harrington, H. Lin, S. V. Berdyugina, J. Trujillo-Bueno, S. L. Keil, & T. Rimmele (San Francisco, CA: ASP), 341
Goode, P. R., Yurchyshyn, V., Cao, W., et al. 2010, ApJL, 714, L31
Hinze 1959, Turbulence: An Introduction to Its Mechanism and Theory (New York: McCraw-Hill)
Hurlburt, N. E., Schrijver, C. J., Shine, R. A., & Title, A. M. 1995, in Proc. of the 4th SOHO Workshop, Helioseismology, ed. J. T. Hoeksema, V. Domingo, B. Fleck, & B. Battrick (Noordwijk, Netherlands: ESA), 239
Jenkins, Watts. 1969, Spectral Analysis and its Applications (San Francisco, CA: Holden-Day)
Kosugi, T., Matsuzaki, K., Sakao, T., et al. 2007, SoPh, 243, 3
Kuzanyan, K. M., Pipin, V. V., & Zhang, H. 2007, AdSpR, 39, 1694
Lites, B. W., Kubo, M., Socas-Navarro, H., et al. 2008, ApJ, 672, 1237
Matloch, Ł., Cameron, R., Shelyag, S., Schmitt, D., & Schüssler, M. 2010, A&A, 519, A52
Matthaeus, W. H., Zank, G. P., Oughton, S., Mullan, D. J., & Dmitruk, P. 1999, ApJL, 523, L93
Monin, A., & Yaglom, A. 1975, Statistical Fluid Mechanics: Mechanics of Turbulence (Cambridge, MA: MIT Press)
November, L. J., & Simon, G. W. 1988, ApJ, 333, 427
Oughton, S., Matthaeus, W. H., & Zank, G. P. 1999, in Proc. of the 8th SOHO Workshop: Plasma Dynamics and Diagnostics in the Solar Transition Region and Corona, ed. J.-C. Vial & B. Kaldeich-Schü (Noordwijk: ESA), 525
Pipin, V. V., Kuzanyan, K. M., Zhang, H., & Kosovichev, A. G. 2011, ApJ, 743, 160
Rüdiger, G., Kitchatinov, L. L., & Brandenburg, A. 2011, SoPh, 269, 3
Strous, L. 1994, PhD thesis, Utrecht Univ., The Netherlands
Strous, L. H., Scharmer, G., Tarbell, T. D., Title, A. M., & Zwaan, C. 1996, A&A, 306, 947
Thomas, J. H., & Stanchfield, I. D. C. H. 2000, ApJ, 537, 1086
Title, A. M., Hurlburt, N., Schrijver, C., Shine, R., & Tarbell, T. 1995, in Proc. of the 4th SOHO Workshop, Helioseismology, ed. J. T. Hoeksema, V. Domingo, B. Fleck, & B. Battrick (Noordwijk, Netherlands: ESA), 113
Tsuneta, S., Ichimoto, K., Katsukawa, Y., et al. 2008, SoPh, 249, 167
Verdini, A., Velli, M., Matthaeus, W. H., Oughton, S., & Dmitruk, P. 2010, ApJL, 708, L116
Verma, M., & Denker, C. 2011, A&A, 529, A153
Verma, M., Steffen, M., & Denker, C. 2013, A&A, in press (arXiv:1305.6033)
Wang, J., Wang, H., Spirock, T., et al. 2000, Proc. SPIE, 4093, 481
Welsch, B. T., Abbett, W. P., De Rosa, M. L., et al. 2007, ApJ, 670, 1434
Wöger, F., & von der Lühe, O. 2007, ApOpt, 46, 8015
Zank, G. P., Dosch, A., Hunana, P., et al. 2012, ApJ, 745, 35